Journal of Geophysical Research: Space Physics

RESEARCH ARTICLE
10.1029/2018JA025642

Unusual Generation of Localized EPB in the Dawn Sector Triggered by a Moderate Geomagnetic Storm

S. Sripathi[1], M. A. Abdu[2], A. K. Patra[3], and R. N. Ghodpage[4]

[1]Indian Institute of Geomagnetism, New Bombay, India, [2]Instituto Tecnológico de Aeronáutica and Instituto Nacional de Pesquisas Espaciais, São José dos Campos, Brazil, [3]National Atmospheric Research Laboratory, ISRO, DOS, Gadanki, India, [4]MF Radar Center, Indian Institute of Geomagnetism, Shivaji University, Kolhapur, India

Key Points:
- We studied the fresh development of EPBs in the dawn triggered by a moderate geomagnetic storm using radar and ionosonde
- The IMF *Bz* southward transitions occurring well after midnight also can produce eastward PPEF in contrast to the hitherto known pattern
- Another finding is that the topside irregularity plume height can be modulated under a correspondingly fluctuating IMF *Bz* values

Correspondence to:
S. Sripathi,
ssripathi.iig@gmail.com

Citation:
Sripathi, S., Abdu, M. A., Patra, A. K., & Ghodpage, R. N. (2018). Unusual generation of localized EPB in the dawn sector triggered by a moderate geomagnetic storm. *Journal of Geophysical Research: Space Physics*, *123*, 9697–9710. https://doi.org/10.1029/2018JA025642

Received 4 MAY 2018
Accepted 14 OCT 2018
Accepted article online 17 OCT 2018
Published online 8 NOV 2018

Abstract An interesting piece of observation related to the equatorial plasma bubble (EPB) that is triggered by a geomagnetic storm at dawn sector on 4–5 February 2011 is presented. The storm activity was initiated at 17 UT when interplanetary magnetic field (IMF) *Bz* turned southward and the *Dst* index started decreasing (accompanied by *AE* intensifications) attaining its minimum at −70 nT. The IMF *Bz* presented large fluctuations marked by southward/northward transitions at slow and rapid rates and eventually returning to normal in the morning of 5 February. Observations from the very high frequency radar located at Gadanki, an off-equatorial station; an all-sky imager located at Kolhapur, a low-latitude station; and an ionosonde at Tirunelveli, an equatorial station, are analyzed to study the impact of this storm on the postmidnight to presunrise equatorial spread *F*. The results demonstrate that EPB irregularities can be generated by penetration electric field during what can be characterized as a moderate storm event. In contrast to prevailing belief, the present results show that EPB/equatorial spread *F* can be generated by undershielding electric field in the dawn sector, caused by an unusually delayed polarity reversal of the penetration electric field. The results further reveal oscillatory behavior in the height of *F* layer topside irregularities in association with IMF *Bz* oscillations. Observation of radar echoes from nighttime *E* layer irregularity structures and their Doppler velocities representing the penetration electric field polarity and intensity are also a notable finding of this paper.

Plain Language Summary An interesting observation related to the equatorial plasma bubble that is triggered in the postmidnight to presunrise period by a moderate intensity geomagnetic storm on 4–5 February 2011 over India is analyzed using the observations from the very high frequency radar located at Gadanki, an off-equatorial station; optical airglow imager at Kolhapur located at low latitude; and an ionosonde at Tirunelveli, an equatorial station. The storm activity was initiated at 17 UT on 4 February 2011 when interplanetary magnetic field (IMF) *Bz* turned southward and the *Dst* index started decreasing and attaining its minimum of −70 nT. The IMF *Bz* showed large fluctuations marked by southward/northward transitions at slow and rapid rates and eventually returning to normal in the morning. In contrast to prevailing belief, the present results show that equatorial plasma bubbles can be triggered by undershielding electric field in the dawn sector, caused by an unusually delayed polarity reversal of the penetration electric field. The results further reveal oscillatory behavior in the height of *F* layer topside irregularities in association with IMF *Bz* oscillations.

1. Introduction

Electrodynamics of the *E* and *F* regions of the nightside ionosphere play a significant role in providing necessary conditions for the generation of equatorial spread *F* (ESF) irregularities (e.g., Fejer & Kelley, 1980; Kelley, 1989; Kelley et al., 2011). Upon initiation at the bottomside of a rising *F* layer these plasma irregularities rise nonlinearly to topside ionosphere and develop into equatorial plasma bubbles (EPBs) through Rayleigh-Taylor (RT) instability mechanism. Past studies have shown that geomagnetic storms either suppress or generate the EPBs depending upon the local time and polarity of the interplanetary electric fields (e.g., Aarons, 1991; Abdu et al., 2003, 2009; Basu et al., 2001; Fejer, 1991; Fejer et al., 1979; Martinis et al., 2005; Ramsingh et al., 2015). Accordingly, the EPB development conditions depend, obviously, on the polarity of these electric fields. The eastward (westward) polarity of an undershielding (overshielding) electric field in the evening hours reverses to westward (eastward) around 23 LT before their respective polarities again reverse in the morning hours as shown from analysis of Republic of China Satellite (ROCSAT) data by Fejer

et al. (2008). As a result, the EPB generation may be triggered (suppressed) by undershielding (overshielding) electric field during post sunset hours, whereas it can be suppressed (triggered) by undershielding (overshielding) electric field during postmidnight-presunrise hours. It should be noted that the postsunset EPB development is strongly dependent on the ways in which the evening prereversal (PRE) vertical drift is impacted by these electric fields, an undershielding electric field of eastward polarity enhancing the PRE while an overshielding electric field suppressing it (e.g., Abdu et al., 2009). On the other hand EPB development can occur during postmidnight-presunrise hours due to anomalous vertical drift arising from overshielding electric field (e.g., Kelley et al., 1979). Since the occurrence of nighttime plasma irregularities in the equatorial *F* region can pose severe threat to satellite communication and Global Navigation Satellite Systems-based navigation systems (e.g., Kelley, 1989; Kelley et al., 1981, 2011; Kintner et al., 2001), it is essential to understand the role of geomagnetic storms on the generation or suppression of these irregularities. Other factors such as atmospheric gravity waves, tides, and planetary waves in addition to solar flux also play significant roles in the day-to-day variability of these plasma irregularities (Abdu, 2016; Kelley et al., 1981, 2011). Accordingly, the understanding of the structure and dynamics of these irregularities and the eventual development of techniques for predicting their occurrences become challenging tasks.

In this paper we address the formation of plasma bubble associated irregularities under unusual conditions surrounding magnetic disturbances during a moderate geomagnetic storm event. It should be understood further that, sometimes, it is difficult to identify the precise nature of the causative factors for the storm-induced variabilities in ESF/EPB irregularity development due to the fact that all the above mentioned factors can occur superposed during extended storm events arising from prolonged or fluctuating interplanetary magnetic field (IMF) *Bz* south conditions. In this paper, we analyze simultaneous very high frequency (VHF) radar, ionosonde, and airglow data during the development of a moderate storm that occurred on 4–5 February 2011. The results demonstrate that though this is a moderate storm, with the *Dst*/*SYM-H* index not exceeding −65 nT, it can still cause significant degree of irregularity development and dynamical changes in its features. The results further indicate that while background ionospheric conditions did not support the generation of postsunset/premidnight plasma bubbles, they can be initiated at postmidnight-predawn sector due to rapid increase in the disturbance zonal electric field of eastward polarity due to undershielding effect associated with *Bz* southward turning. Different from results so far known, there is evidence that the polarity of undershielding electric field continued to be eastward even well after its nominal westward reversal time reported to be around 23 LT.

While significant studies have been made during both quiet and disturbed periods using radars in the American sector (e.g., Fejer & Kelley, 1980; Fejer et al., 1990; Hysell & Burcham, 1998, 2002; Woodman & LaHoz, 1976), such studies were initiated in the recent past in the Asian sector using the Mesosphere-Stratosphere-Troposphere (MST; VHF) radar located at Gadanki in India (e.g., Rao et al., 1995) and Equatorial Atmosphere Radar (EAR) located in Indonesia (e.g., Fukao et al., 2003). Since the Indian MST radar is usually scheduled for campaign modes of operation mostly from 18:00 to 02:00 of the next day, limited observations were available to investigate the storm-triggered plasma bubble development in the dawn sector. Chakrabarty et al. (2006) investigated the radar observations of storm-triggered EPBs in the postsunset sector over Indian longitude. More recently, Patra et al. (2016) studied the generation of premidnight plasma irregularities during the St. Patrick's Day geomagnetic storm of 17 March 2015. Due to uninterrupted operations of the EAR radar that was established in 2001, few examples of storm-triggered postmidnight plasma bubbles have been reported (e.g., Fukao et al., 2003; Ram et al., 2015). However, no study has been reported on storm-induced plasma bubble development in the dawn sector over Indian longitude. In the recent past, the Gadanki MST radar has been operating in the postmidnight sector that has permitted the study of late night plasma bubble irregularities and their sources (e.g., Patra et al., 2009).

In addition to radio experiments, optical airglow observations such as all-sky imagers (ASIs) have also been widely used to study the variability of EPBs and their zonal drifts during both quiet and disturbed periods (e.g., Abalde et al., 2009; Pimenta et al., 2007; Paulino et al., 2010). As these zonal drifts are known to reverse direction from eastward to westward during geomagnetic storms due to changes in the thermospheric winds, these optical imagers are widely used to monitor the zonal movements of these EPBs in order to study the changes in thermospheric zonal winds. Paulino et al. (2010) investigated the nighttime zonal drifts of EPBs using optical airglow emissions based on large number of EPB events and suggested that westward zonal drifts do occur on quiet days as well; however, their numbers are quite small, outside of

Table 1
Radar Experimental Parameters Used for Spread F Observations

Parameter	Value
Radar frequency	53 MHz
Transmitter peak power	2.5 MW
Antenna beam width	3°
Antenna	32 × 32
Antenna gain	36 dB
Beam direction	15°N off zenith
Pulse width	16 μs
Coded	Uncoded
Interpulse period	5 ms
Number of coherent integration	1
Number of FFT point	256
Number of spectral averaging	8
Velocity window	±283 m/s
Range resolution	2.4/4.8 km
Velocity resolution	2.25 m/s

Note. FFT = fast Fourier transform.

geomagnetically active periods. In this paper we report a unique observation of storm time triggering of localized plasma bubble irregularities in the dawn sector over India that is found to be initiated under anomalous conditions during a moderate storm using ground-based multi-instrument and multisite observations.

2. Details of the Instruments and Data Processing

A strong solar wind with a cloud of coronal mass ejection hit the Earth's magnetopause during late hours on 4 February 2011, which produced a G2-class (*Kp* = 06) moderate geomagnetic storm. The ionospheric response to this storm is studied using geomagnetic indices *SYM-H* and *AE* (*AU*/*AL*) and high-resolution solar wind and IMF parameters measured by Advanced Composition Explorer satellite time shifted to magnetosphere boundary (bow shock).

The observations presented here were made by the Indian MST radar located at Gadanki (13.5°N, 79.2°E, dip latitude: 6.3°N; e.g., Rao et al., 1995). The radar parameters used for the observations presented here are listed in Table 1. The observed data are in the form of signal-to-noise ratio, Doppler velocity, and spectral width as a function of height and time. Ionosonde observations were made at Tirunelveli (8.73°N, 77.7°E, magnetic latitude: 0.23°N), an equatorial station in the southern part of India. The ionosonde, which is a CADI (Canadian Advanced Digital Ionosonde; e.g., Grant et al., 1995) setup in the year 2006 (see Sripathi et al., 2016), can operate both in ionogram and drift modes. In the ionogram mode, it sweeps through the sounding frequencies usually from 2 to 16 MHz with resolution of a few kilohertz to produce one ionogram at every 10-min interval. In the drift mode the CADI operates at a few selected fixed frequencies at a high (1-min) temporal resolution. The ionograms and drift modes of observations so obtained were analyzed/scaled to study the *F* layer height variations and spread *F* characteristics over the equator on 4–5 February 2011.

In addition, we also analyzed data from night airglow observations at OI 630 and OI 557 nm and OH emission using ASI and multispectral photometer at the low-latitude station Kolhapur during this storm. The nights of the observations may be characterized as moonless clear-sky nights. Six thin film-coated interference filters are used in the filter wheel to allow the transmission of OI 630, OI 557.7, OH 840, and OH 846 nm, OH Meinel bands at 720–910 nm, and the background sky noise at 857 nm. The typical bandwidth of the filters except the OH Meinel bands is 2 nm approximately. The OI 630-nm data were obtained from dusk to dawn using integration time of 120, 120, 06, 06, 90, and 10 s, respectively. A high-resolution (1,024 by 1,024 pixels) charge-coupled device chip was used to capture the image of the sky with nearly 180° field of view. Before the operation, dark noise counts were reduced by thermoelectrically cooling of the charge-coupled device to −80 °C. The filter wheel and camera shutter were controlled by a computer. More details of the experimental setup are described in Ghodpage et al. (2014).

3. Results

Figures 1a and 1b show, respectively, the temporal variations of the solar wind velocity and the IMF *Bz* (blue) and interplanetary electric fields (red), on 4–5 February 2011. Figures 1c and 1d show, respectively, the corresponding variations in the auroral electrojet activity index (*AE*) and the *SYM-H* (*Dst* index). On 4 February the solar wind showed a step-like increase at ~2:40 UT to ~380 km/s remaining so till another step increases at ~13:20 UT when the speed attained ~410 km/s and remained nearly steady till ~19:10 UT. A third step-like increase occurred at this time, which was followed by a steady increase reaching a value of 600 km/s by 02 UT, which continued till almost the end of 5 February. We note that the step-like increase at 02:40 and 19:10 UT was accompanied by short durations of (V-shaped) IMF *Bz* southward excursions, whereas the second increase (at 13:20 UT) was accompanied by northward excursion in *Bz* to ~12 nT. The subsequent decrease in *Bz* continued till its southward reversal at ~17 UT that marked the onset of the major activity of the day characterized by a large increase in *AE* (attaining ~1,300 nT). After a transient northward increase, the *Bz* again turned southward at 19:30 UT attaining a minimum value of −20 nT at ~20 UT, which resulted in

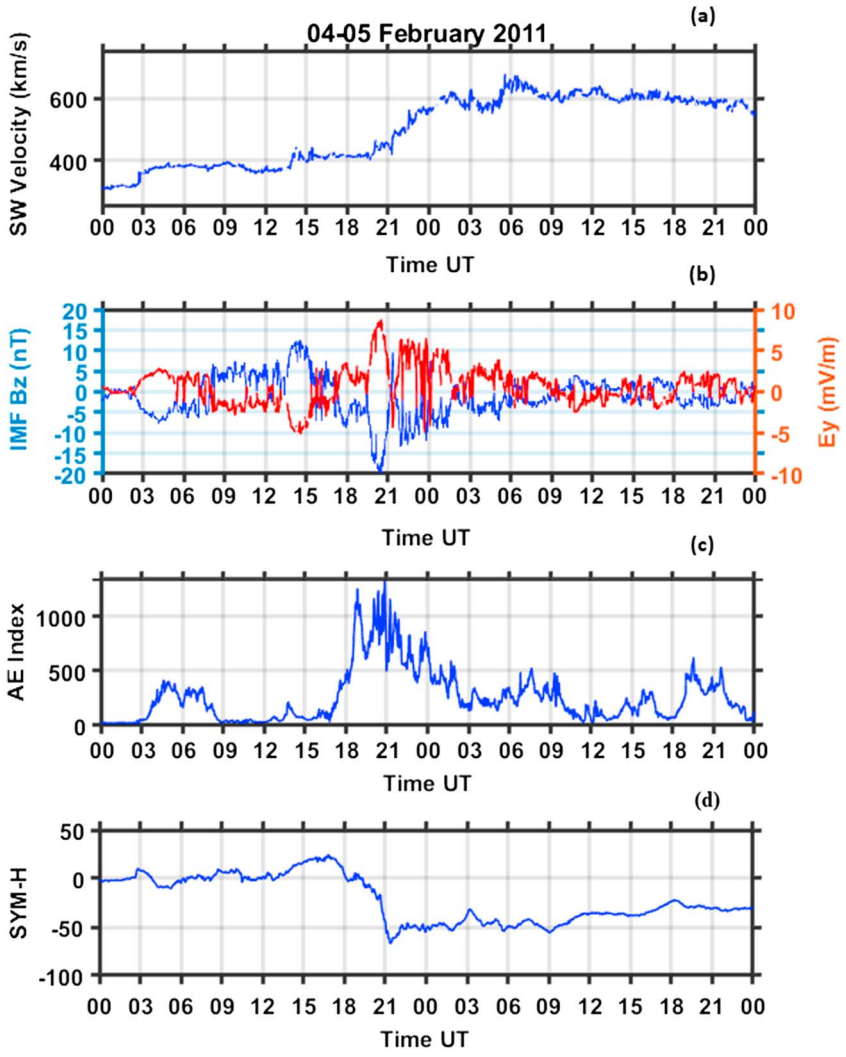

Figure 1. Panels from top to bottom: (a) SW velocity, (b) the IMF (*Bz*), (c) the auroral electrojet (*AE*) index, and (d) the *SYM-H* representing 1-min *Dst* values, during 4–5 February 2011. SW = solar wind; IMF = interplanetary magnetic field.

enhanced *AE* activity peaking near 21 UT followed by gradual decrease superposed by rapid fluctuations that continued with variable intensity till the end (of the data). The solar wind speed remained nearly steady with only small variations in the *Bz* during this period. The increase in *ASY-H*/*Dst* (beginning at ~13 UT) indicative of magnetospheric compression appears to coincide with the second step-like increase in the solar wind speed that occurred at 13:20 UT (mentioned above) when the *Bz* increased northward. The *SYM-H*/*Dst* decrease that marked the storm onset corresponded to the *Bz* southward turning just after ~17 UT. The subsequent intensification of the storm (due to the *Bz* southward turning at 19:30 UT) was characterized by rapid decrease in *SYM-H*/*Dst* to reach a minimum value of −63 nT at ~21:30 UT, which qualifies this event as a moderate magnetic storm based on *Dst* classification (e.g., Loewe & Prölss, 1997). The responses to these disturbances extending to the postmidnight/presunrise hours over India, leading to plasma bubble/ESF irregularity generation under anomalous conditions of the penetration electric field, are discussed below.

3.1. *E* and *F* Layer Responses to the Disturbance Electric Fields

Figure 2 shows, starting from 12 UT on 4 February, the dynamic changes in the ionospheric parameters as registered by the Gadanki radar and Tirunelveli CADI presented together with the disturbance variations in the IMF *Bz* and *SYM-H*/*Dst* indices. In Figure 2a the IMF *Bz* shows (beginning at 12 UT) large degree of variations, at time scales of a few hours superposed by transients of a few minutes (to a few tens of minutes)

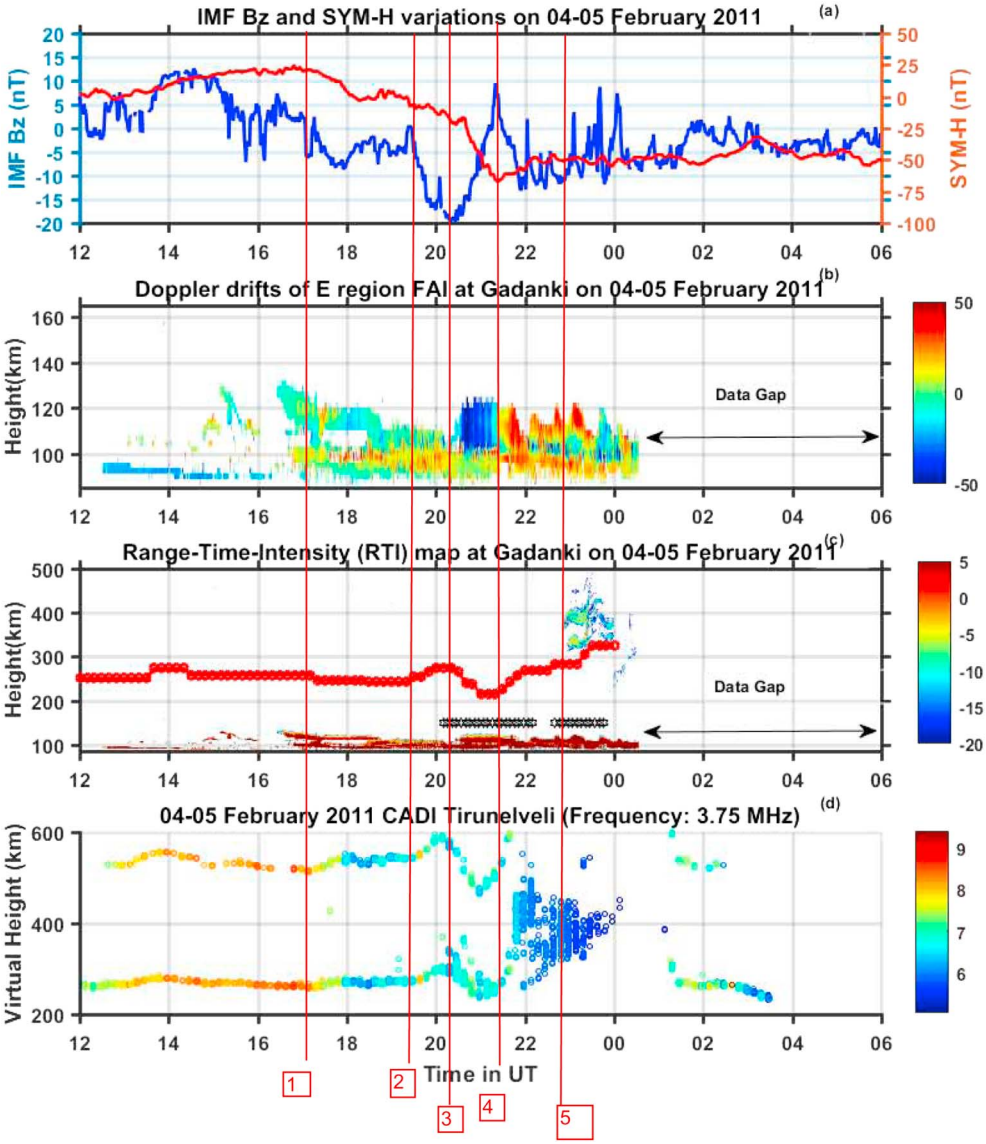

Figure 2. Variations in different geophysical and ionspheric parameters highlighting the storm disturbance period on 4–5 February 2011. (a) The IMF *Bz* and *SYM-H* indices. (b) The range-time map showing the Doppler velocity variation (RTD map) in the *E* region as obtained from the very high frequency radar at Gadanki. (c) The range-time-intensity map over Gadanki in which are overlaid the *h*′*F* (km) variation (red curve) and spread *F* duration (in black hexagons) from CADI ionosonde over Tirunelveli. (The lowest trace in brown is the *E* region trace of the radar RTI). (d) The virtual height at 3.75 MHz, showing also the range spreading echoes, over Tirunelveli. Note that the first and second hop traces are present. IMF = interplanetary magnetic field; RTD = range-time-Doppler; CADI = Canadian Advanced Digital Ionosonde; RTI = range-time-intensity.

during which several north-south polarity reversals occurred, some of which, of present interest to us, are identified by vertical lines. Figure 2b shows the range-time-Doppler velocity map of 2.83-m irregularities in the *E* region recorded by the Gadanki radar, which is a height expanded version of the *E* layer echo trace shown also in Figure 2c, and Figure 2c shows range-time-intensity map covering *E* and *F* regions extending up to 500 km, in which are overlaid the *F* layer base virtual height (*h*′*F*) variation and the duration of range type spread *F* traces, the detailed characteristic of which at 3.75 MHz with the corresponding virtual height variation is shown in Figure 2d. Beginning at 12 UT on 4 February the *Bz* remained mostly northward (interrupted by a few cases of short duration southward transients) till about 17:00 UT when it rapidly turned southward (vertical line 1). After the initial transient it remained southward for a longer duration, presenting also significant fluctuations. Following this first southward turning of the *Bz* (at 17:00 UT which corresponded to 22:30 LT), the *E* layer echoes (in Figure 2b) that were

already in development became intensified indicating also dominantly upward Doppler velocities of the irregularities. This response to the *Bz* southward turning would suggest the role of a prompt penetration electric field (PPEF) of eastward polarity operating in competition with the westward dynamo electric field of normal nighttime ionosphere. The presence of the eastward PPEF is further evident in the simultaneous small increase in the *F* layer height (at 3.75 MHz) clearly observable (starting at the vertical line 1) in Figure 2d. The second episode of the *Bz* southward turning (identified by vertical line 2) that occurred at ~19:30 UT, that is, at ~01:00 LT, also caused significant upward increase in the radar Doppler velocity of the *E* region echoes over Gadanki as well as increase in the *F* layer heights over Tirunelveli. This feature, again, shows the impact of a PPEF, which is an undershielding electric field of eastward polarity due to the *Bz* south condition. (It is relevant to point out that the *E* layer over Gadanki is field line mapped to dip equatorial *F* layer over Tirunelveli.) The *F* layer uplift has resulted in instability growth to which we will return later. The subsequent rapid recovery of the *Bz* south starting at ~20:20 UT (~01:50 LT; identified by the vertical line 3) leading to its eventual reversal to northward calls our attention. During this phase a strong overshielding electric field should be present at equatorial and low latitudes. We may note that this is a westward electric field as evidenced by the enhanced downdraft (negative Doppler velocity) of the *E* layer irregularities (Figure 2b) accompanied also by the rapid descent of the *F* layer (as seen in the layer height decrease) in Figures 2c and 2d. The next important episode is the *Bz* turning south marked by the vertical line 4 at ~21:30 UT (03:00 LT), which is promptly followed by large updraft (positive Doppler velocity) of the *E* region irregularities (Figure 2b) accompanied also by rapid rise of the *F* layer in Figures 2c and 2d. In the presence of continuing *Bz* south condition, though interspersed by short duration northward *Bz* transients, the *E* layer irregularity Doppler velocity remained dominantly upward and *F* layer height continued its ascent till sunrise, which also corresponds to the end of the radar data at ~00:30 UT (06 LT).

The degree of the disturbance variation in the *F* layer height on this night (4–5 February) can be assessed from Figure 3a wherein we have compared this variation with that of the five quietest days of the month whose mean and standard deviation are also shown in the figure. We may note that the quiet time pattern of $h'F$ variation peaks around 14:15 UT, that is, 19:45 LT which corresponds to the evening PRE vertical drift attaining 0 in its reversal after its peak value that usually occurs around 13:30 UT, that is, at ~18:00 LT. In comparison to this, the $h'F$ value on 4 February (the red curve) does not show any notable enhancement, thereby indicating a reduced PRE vertical drift. This reduction of the PRE appears to be due to a westward disturbance electric field associated with *Bz* northward increase (Figure 3b) producing an overshielding electric field (see Abdu et al., 2009). (The variation in the *AE* characterized by its small increase suggesting a weak substorm followed by a recovery phase appears to support this.) A possible PRE suppression due to a disturbance dynamo electric field (DDEF) is unlikely in this case since the *AE* activity that preceded the evening was perhaps not intense enough for that. The *AE* activity (Figure 3c) became rather intense starting from 17 UT (22:30 LT). As a result of this enhanced *AE* activity, and due possibly to the dominant role of a resulting DDEF, the $h'F$ that started its increase at ~21:30 UT (03:00 LT) that was initiated by an eastward PPEF (as mentioned before) must have continued its ascent till 00 UT (05:30 LT; Figure 3a). It is well known that the DDEF has eastward polarity at these local times (Blanc & Richmond, 1980; Fejer et al., 2008).

3.2. ESF/EPB Irregularity Development Due to Disturbance Electric Fields

As mentioned earlier the irregularities first developed in the *E* region on the night of 4 February, starting from sunset, as may be noted in Figure 2b, and under conditions of the magnetospheric disturbances indicated by the variations in IMF *Bz* and *SYM-H* indices. Initially, only weak *E* region echoes were present from 12:00 to 17:00 UT which are mainly arising from lower *E* region Field Aligned Irregularities (FAI). Starting from around 17:00 UT with the *Bz* turning south, the radar echoes are seen at multiple altitudes in the *E* region corresponding to different layers of irregularity structures, but no irregularity development was observed in the *F* region. After 19:15 UT, marked by more intense *Bz* south conditions, and until 00:00 UT, the radar *E* layer echoes became more intense having larger Doppler velocities, also presenting dynamic changes in the layer structuring. These changing Doppler velocities are, in general, a useful indicator of how the changing polarity of the disturbance electric field impacted the ESF irregularity development (as we will discuss soon). No radar echo from the *F* region was received until 23:30 UT (Figure 2c). The near-total reduction of the PRE vertical drift, as described above, must be the cause of the complete absence of the radar echoes and the ionogram spread *F* irregularities during the postsunset period on this evening. Later in the night, however,

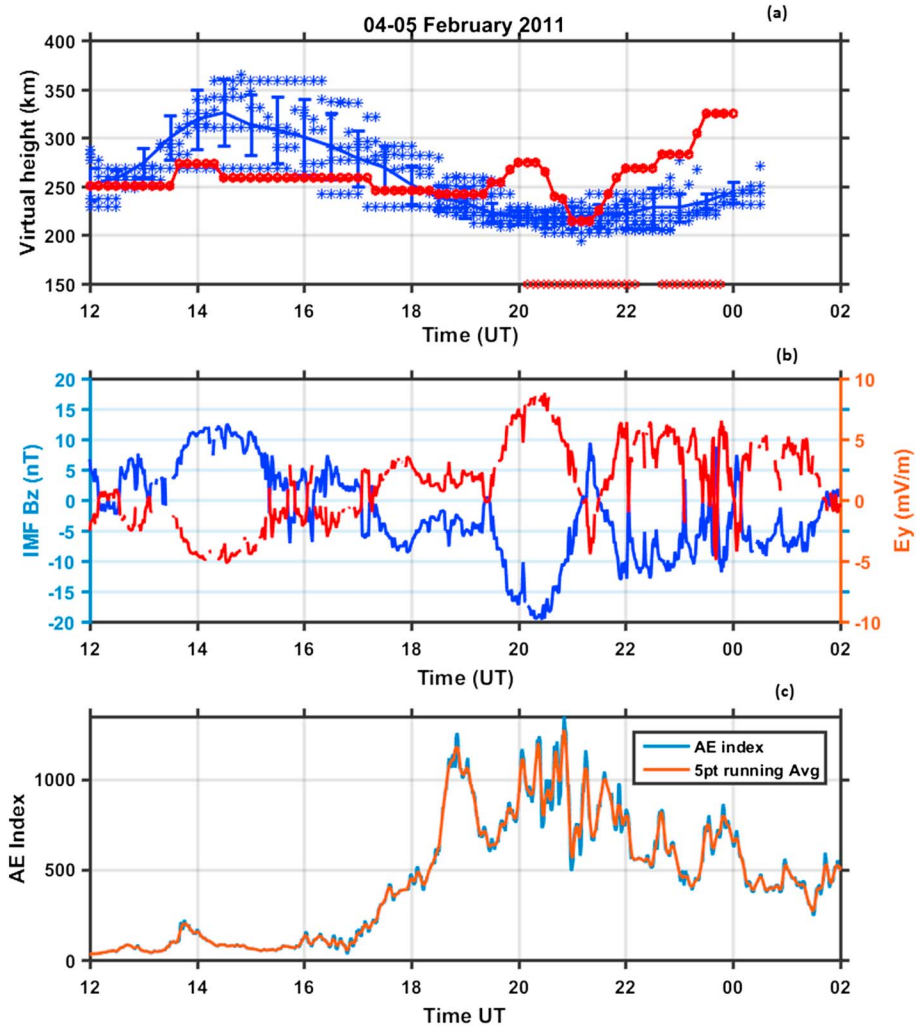

Figure 3. From top to bottom: (a–c) The temporal variation of (a) *h′F* (km) on 4–5 February 2011 along with its variation on five international quiet days over Tirunelveli, with the mean (solid line) and standard deviation (vertical bars) also shown. (b) Variation in IMF *Bz* component and in the corresponding *y* component of the IEFy and (c) *AE* index and its five-point running mean values. IMF = interplanetary magnetic; IEFy = interplanetary electric field.

postmidnight ESF irregularities developed over Tirunelveli, observed in the form of weak range spreading echoes at 3.75 MHz starting at ~20 UT (01:30 LT; Figure 2d). This was produced by the *F* layer height increase due to a PPEF of eastward polarity associated with the *Bz* southward turning that occurred at ~19:20 UT (00:50 LT) indicated by the vertical line 2 in Figure 2. The spread *F* echoes are found to be decaying with the descent of the *F* layer that occurred in consonance with the *Bz* south condition and its turning north (between vertical lines 3 and 4 in Figure 2). It appears to be clear that a westward electric field arising from the overshielding effect associated with the *Bz* turning north is responsible for the descent of the layer that caused the weakening of the irregularities. (As pointed out earlier the overshielding westward electric field is clearly observable in the downward Doppler velocity of the *E* layer FAI at this time; Figure 3b.) Continuing with the sequence, notice that the rapid southward turning of the *Bz* that occurred at 21:30 UT (indicated by the vertical line 4 in Figure 2) and the associated PPEF of eastward polarity are responsible for the *F* layer ascent, which resulted in renewed irregularity development indicated by the enhanced range spreading echoes that continued till 00 UT when the data ended near sunrise. After ~22:50 UT, suddenly the radar started observing echoes from the *F* region at multiple altitudes ranging from 320 to ~450 km (Figure 3c). These echoes are much weaker than the *E* region echoes. However, these echoing regions appear to be raising and falling FAI structures, presenting a degree of height oscillation (to be discussed later). There is another echoing region that can be seen in

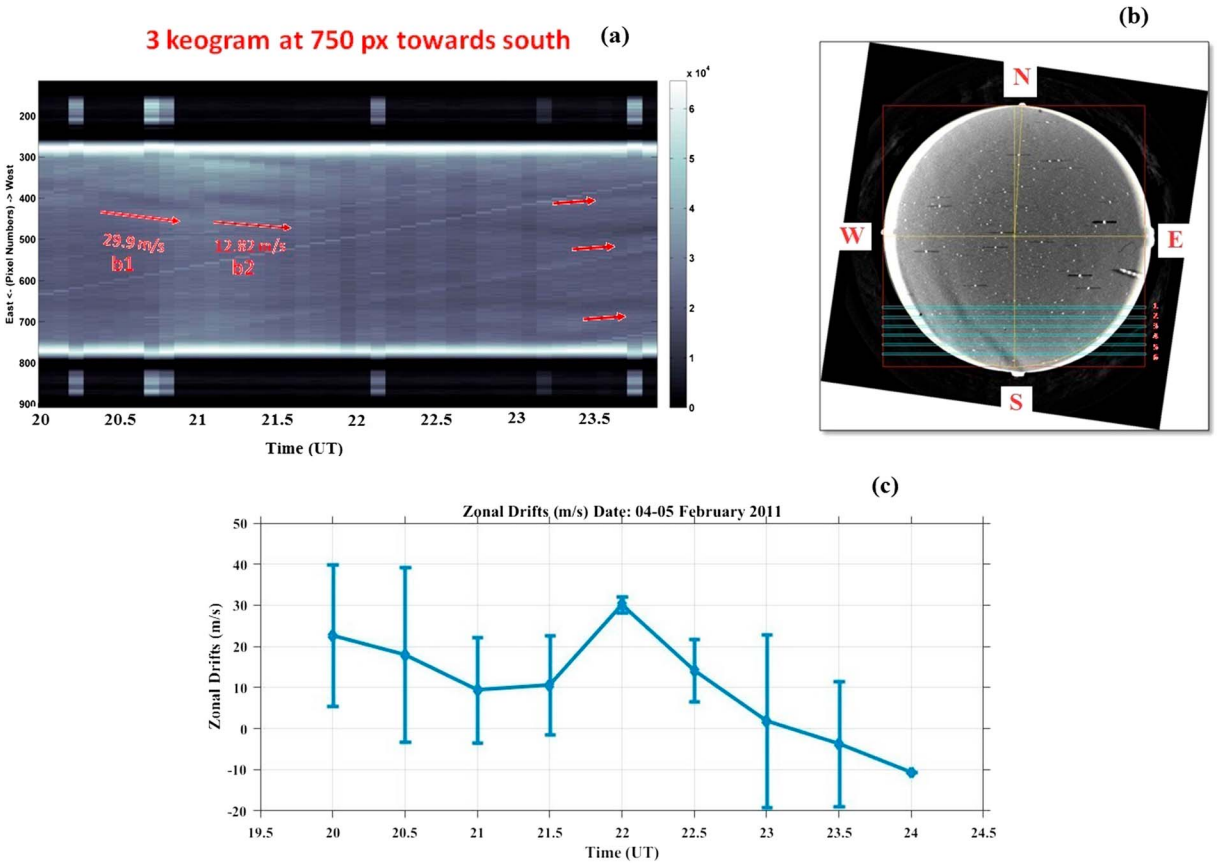

Figure 4. (a) The keogram map of all-sky imager observations at OI 630 nm, (b) the all-sky imager observations of EPBs, and (c) the temporal evolution of zonal plasma drifts on 4–5 February 2011. EPB = equatorial plasma bubble.

the radar map at 00:00 UT which is very weak in its strength, but it rises very fast from ~230 to 300 km in a span of 30 min suggesting a rise velocity of ~40 m/s. It may be noted that radar was operated until 00:30 UT (06:00 Indian Standard Time) of 5 February 2011.

We may now discuss the OI 630.0-nm ASI observations at Kolhapur station located at low latitude during the same night. The results are shown in Figures 4a–4c in the form of keogram maps and zonal drift velocity of the EPB structures. Figure 4b shows a sample ASI image in OI 630.0-nm emission recorded on 4–5 February 2011 at 02:28:55 Indian Standard Time, while Figure 4a shows the keogram map as obtained from the longitudinal displacement of the ASI imager at a specific latitude. Figure 4c shows the temporal variation of zonal drifts as obtained from the keogram maps. The imager pixel size is 1,024 × 1,024. The circle in which OI 630.0-nm emission is recorded is of 140° field of view. The white edges are the local light interference. The blue horizontal bars shown in ASI image in the southern part are the east-west 20-pixel strip for intensity extraction which are further used to construct keogram as shown in Figure 4a. The EPBs onset occurred in the airglow imager at around 20:30 UT, at local midnight hours, quite similar to ionosonde observations. So this observation also suggests that the EPBs are generated at local midnight and not drifted in from other location. The drift velocity (Figure 4c) shows that initially this EPB was drifting east with mean drift velocity of ~20 m/s. But the eastward velocity gradually reduced until 21 UT when it started increasing eastward and peaked at 22 UT before it again started reducing its velocity, which eventually turned westward in the early morning hours. We also examined the gravity wave activity in the OH Meinel band emissions in the mesospheric during the same night. But we did not detect any gravity wave activity prior to the ESF onset. This suggests that the wavy structure as seen in the form of the height oscillations was not the continuation of any perceivable gravity waves activity in the mesosphere/lower thermosphere region.

Since the ionosonde and OI 630-nm emission data are limited to the *F* layer bottomside only, while the radar data connect the observation to topside of *F* layer, we may examine how the multiobservations that measure

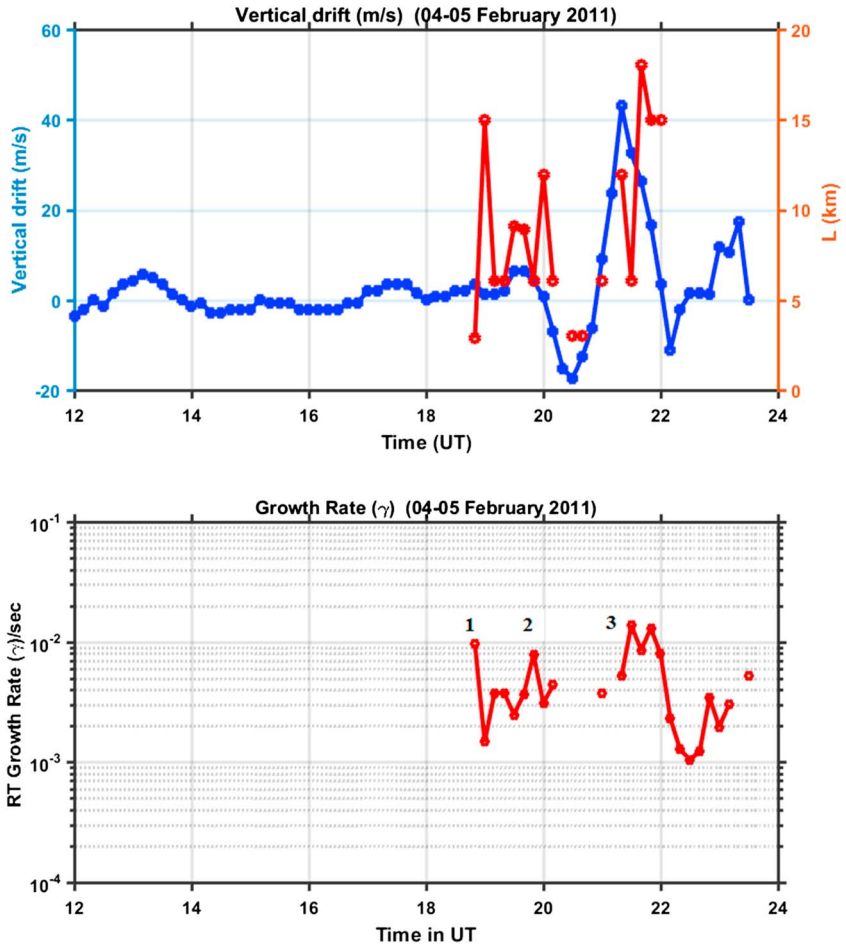

Figure 5. Variations in the (top) vertical drift velocity calculated as d$h'F$/dt over Tirunelveli and the F layer bottomside scale length and (bottom) RT instability growth rate based on the parameters in (top panel). RT = Rayleigh-Taylor.

different altitudes may help us understand the possible dynamics of the irregularity development sequence that was triggered by the 21:30 UT *Bz* southward episode. Figure 5 shows the variation in RT instability linear growth rate calculated using the F layer height and layer bottomside gradient scale length obtained from ionograms on the night of 4–5 February. Two fixed plasma frequencies, namely, 2.5 and 3.0 MHz, were used to obtain the gradient scale length and the corresponding layer height as was done by Subbarao and Krishna Murthy (1994). This method is frequently used to obtain the parameters used in the RT growth rate calculation. We calculated the ion-neutral collision frequency using neutral density and temperature obtained from the Mass-Spectrometer-Incoherent-Scatter (MSIS) model (e.g., Picone et al., 2002). The growth rate (γ) of the linear RT instability in its simplified form is given as follows:

$$\gamma = \frac{1}{L}\left(\frac{g}{\vartheta_{\text{in}}} + V\right) - \beta$$

where $L^{-1} = \left(N^{-1}\frac{dN}{dh}\right)$ is the inverse gradient scale length, N = electron density/cm^3, h = height (km), g = acceleration due to gravity (m/s^2), υ_{in} is the ion-neutral collision frequency, V = vertical drift in meters per second, and β is the recombination rate. In the above equation, the first term indicates the growth due to gravity term, while the second term shows the contributions due to vertical drifts. The last term represents damping term arising from recombination.

We may note three major peaks in the growth rate values exceeding 7×10^{-3} s^{-1}, marked 1, 2, and 3 that strongly indicate irregularity generation (with growth time $<$ ~150 s). The first of these peaks appears to

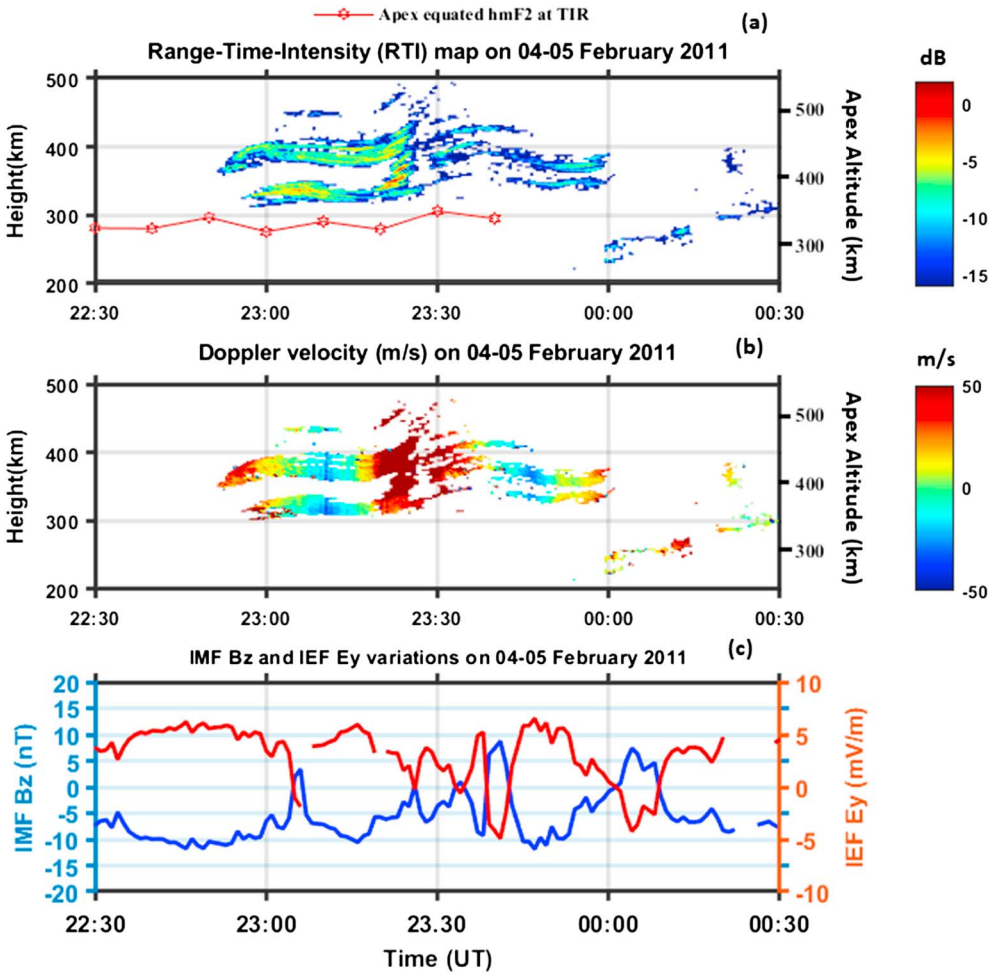

Figure 6. Zoomed-in pictures of (a) radar RTI and (b) RTD maps, and (c) the IMF *Bz* and IEF variations, from 22:30 UT (03:00 LT) to 00:30 UT (06:00 LT). The red curve in (a) is the h_mF_2 over Tirunelveli shown at apex altitude on the right side scale. RTI = range-time-intensity; RTD = range-time-Doppler; IMF = interplanetary magnetic field; IEF = interplanetary electric field.

correspond to the very weak range spread echoes seen around ~19:00 UT (00:30 LT; near the vertical line 2, in Figure 2), which decayed rapidly. The second peak in the growth rate appears to correspond to the generation of the irregularity patch that produced the range spread echoes at ~20:10 UT (01:40 LT; close to the vertical line 3). With the rapid descent of the layer to lower heights (reaching ~220 km) under the overshielding westward electric field, these irregularities also decayed rather rapidly. The largest of the peaks (peak 3) occurred around 21:30 UT (03:00 LT), which appears to be responsible for the more intense Spread F (SF) irregularities that produced the strong range spreading echoes beginning at ~21:40 UT (03:10 LT) that persisted till 00 UT (05:30 LT) close to sunrise. This strong range spreading echoes might indicate generation of irregularities that evolved into vertically rising bubble structures so that the radar plume that appeared at ~22:50 UT (04:20 LT; Figure 2c) might represent the *F* layer topside bubble signature (The h_mF_2 variation plotted in Figure 6 to be discussed later does attest to its characterization as topside bubble irregularities.) The delay of about 70 min observed in the appearance of radar echoes with respect to the onset of the ionogram Range spread F (RSF) trace could be attributed to the separation in latitude (dip angle) and longitude between the two observing locations. Tirunelveli being located at (close to) magnetic dip equator, the radar echo when projected onto equatorial apex height is found to be located (at the onset time) at a height ~80 km higher than that of the ionogram RSF trace (referred to the *F* layer bottomside). If the delay of 70 min in the radar echoes (with respect to the onset time of the spread *F* echoes) is attributed to the rise velocity of the bubble vertical growth, then the corresponding bubble rise velocity can be estimated to be about 20 m/s, which represents a very slow bubble growth

rate. From model simulation of bubble growth under typical post sunset condition, the bubble vertical rise velocity has been found be ~200 m/s (e.g., Zalesak et al., 1982). Perhaps under the postmidnight/presunrise conditions, the prevailing disturbance electric field might be conducive to only slower bubble growth rate and hence smaller rise velocity as found in this case. Another possible cause of the delay in the radar plumes may be sought in the longitudinal separation of the two sites. The radar located some 165 km east of the CADI might detect the radar echoes after some delay if the irregularities generated over Tirunelveli propagated eastward. The corresponding eastward velocity can be estimated as ~40 m/s. However, the zonal drift velocity of the bubble irregularities at the local time of their observation, that is, around 03–04 LT, is extremely small and even turned to westward as seen in the EPB drift velocity shown in Figure 4 (see, e.g., Abdu et al., 1985), which therefore may rule out the possibility of the delay being caused by longitudinal separation. Thus, we may conclude that the PPEF of eastward polarity that occurred at 21:30 UT (03:00 LT) was indeed responsible for the bubble irregularity development presenting very slow vertical growth rate during the presunrise hours of 5 February.

We also examined the VHF scintillation at Tirunelveli, which also suggests that scintillations are observed only in the early morning hours of 5 February. But it may be noted here that Global position system (GPS) L-band scintillation was not detected either in the premidnight or postmidnight sector during this storm in the Indian sector. Since the GPS L-band scintillation is sensitive to intermediate scale size irregularities (e.g., 300–400 m), a weakening or disappearance of the scale sizes of a few hundred meters (e.g., Sripathi et al., 2008) combined with the lower background plasma density of equatorial region (closer to the EIA trough region) might result in the absence of L-band scintillation. It may further be noted that the EAR radar in Indonesia (located eastward of Gadanki by ~21°) ahead in local time by 1 hr 30 min did not detect any irregularity development during this event, which may perhaps be due to the proximity to the sunrise conditions prevailing over there. It is important to recall that storm-associated presunrise bubble generation has been detected in the past over the EAR radar (Fukao et al., 2003).

4. Discussions

The episodes of the IMF *Bz* polarity reversals, accompanied by *AE* activity intensifications and *SYM-H*/*Dst* decrease, representing a moderate magnetic storm, have clearly demonstrated the presence of penetration electric fields, of both the undershielding/overshielding types, in the equatorial low-latitude ionosphere over the Indian sector. These electric fields have produced their characteristic impacts in *E* and *F* region plasma irregularity generations. We noted that the dynamic changes in Doppler velocities of the nighttime *E* layer plasma irregularities, observed by the radar, could serve as a powerful indicator of the polarity of the PPEF as verified also in the *F* layer height responses to these electric fields as observed by the CADI. Although postsunset ESF irregularities were weakened, due possibly to an overshielding westward electric field and/or by a DDEF, the PPEF episodes that occurred in the postmidnight/presunrise period produced ESF irregularities evolving into topside radar plume event. The anomalous nature of the PPEF responsible for the bubble irregularity development (to be explained below) constitutes a notable point of this paper. Plasma bubble development due to penetration electric field occurring during postmidnight/presunrise hours as observed over Jicamarca (Peru) was reported by Kelley et al. (1979), who interpreted the bubble generation as caused by an overshielding electric field of eastward polarity associated with an IMF *Bz* northward turning episode. In this context we may recall that the polarity of the disturbance time undershielding (overshielding) electric field reverses from eastward (westward) to westward (eastward) around 23 LT in most seasons (the latest reversal time being ~01 LT during equinox) as found in the seasonal average pattern of their variation obtained from statistical analysis of ROCSAT-1 plasma vertical drift data by Fejer et al. (2008). These polarity reversal times are also in reasonable agreement with results from global convection models (Fejer et al., 1990; Senior & Blanc, 1984).

The polarities of the penetration electric fields (associated with the IMF *Bz* reversals) observed in the present results do not agree (in most part) with the model-predicted, and so far observed, pattern. For example, the *Bz* turning south that occurred at 17:00 LT for which the PPEF polarity was eastward (vertical line 1 in Figure 2) is in perfect agreement with satellite observations and model results mentioned above. The second episode of *Bz* transitioning to south that occurred at 01:00 LT accompanied also by an undershielding PPEF of eastward polarity (vertical line 2) is marginally in agreement with the expected behavior according to the

delayed polarity reversal time of ~01 LT for equinoctial month obtained by Fejer et al. (2008). This eastward PPEF produced *F* layer rise that was responsible for the development of bottomside range spread *F* of weak intensity. However, the next episode of *Bz* transitioning to north that occurred from 01:45 to 03:00 LT (vertical lines 3 and 4) that produced a strong overshielding electric field of westward polarity causing rapid downdrift of *E* layer irregularities and *F* layer descent does not conform to the expected pattern that predicts overshielding electric field of eastward polarity at these local times (such as that found by Kelley et al., 1979). The rapid descent of the *F* layer down to close to 200 km (real height) caused the rapid decay of the spread *F* irregularities for this case.

The subsequent rapid southward turning of the IMF *Bz* starting at 03:00 LT (vertical line 4) then resulted in an undershielding PPEF of eastward polarity that caused a renewed updraft of the *E* layer echoes accompanied by *F* layer uplift that lead to prompt development of intense bottomside spread *F*, which soon evolved into rising topside bubble structure observed as radar echoes ~70 min after the initiation of the bottomside irregularities. This event sequence represents perhaps the most significant manifestation of the presunrise PPEF during this storm event. In this case again, the polarity of the undershielding electric field does not agree with its expected pattern, which is a westward polarity at this local time. The occurrence of eastward polarity of an undershielding electric field till 03:00 LT as observed here is an anomalous feature to be reckoned with. The continuing rapid changes in the IMF *Bz* that were dominantly southward but marked by transients of northward excursions produced further modulations on the *F* layer height and in the radar echo structure. A zoomed-in picture of the radar image and the simultaneous h_mF_2 and IMF *Bz* variations during this period are presented in Figure 6. The right side axis of Figures 6a and 6b, marked in equatorial apex height, applies to the radar image as well as the h_mF_2 values. We note that the radar plume indeed represents topside bubble signature. Note that Figures 6a and 6b are, respectively, the echo intensity (range-time-intensity) and echo Doppler velocity (range-time-Doppler) maps. We may notice the presence of a quasiperiodic (sinusoidal) oscillation with approximately half hour period modulating the radar echo height. This oscillation might appear to be induced by a continuation of an upward propagating gravity wave, which could have seeded the SF irregularities first observed at the *F* layer bottomside (Figure 2d). Such a possibility, however, is unlikely since the quasiperiod (30 min) of this oscillation is below the characteristic gravity wave period for the thermosphere (e.g., Hines, 1960, Klostermeyer, 1969). More realistically, a comparison between the Doppler velocity variation (Figure 6b) and the IMF *Bz* oscillations (Figure 6c) appears to present a clear correlation. The southward increases in *Bz* are coincident with the negative Doppler velocity indicating a downdraft of the irregularities. In the same way the northward excursions appear well correlated with positive updraft of the irregularities. In these cases the *Bz* southward increases and northward increases, respectively, indicate increases in undershielding electric field with westward polarity and overshielding electric fields eastward polarity. Thus, we note that the bubble irregularities, initially generated by a *Bz* southward turning episode (at vertical line 4, Figure 2), while evolving into topside bubble irregularities, undergo (oscillatory) modulation by the continuing fluctuations in IMF *Bz*. This is the first case being reported of bubble irregularity height being modulated by penetration electric fields. In the PPEF (oscillatory) variations just discussed above that occurred after 04:00 LT, the polarities of the undershielding and overshielding electric fields are back to being in perfect agreement with their expected behavioral pattern. Putting it plainly, the undershielding/overshielding electric field polarity reversal that usually occurs near midnight as per the model and observational results so far reported occurred at a significantly later local time during the storm of 4–5 February 2011. Considering the event sequences just described, it appears that the local time of the polarity reversal of the PPEF occurred by about 04:00 LT during the present storm event. We may point out here that this is the first reporting of the case of a very late (presunrise) polarity reversal of nighttime disturbance electric field during a storm event. It is relevant to note that the PPEF of the undershielding and overshielding types is usually described, respectively, as being dawn-dusk and dusk-dawn oriented. However, the precise local times of the polarity reversals at dawn and dusk meridians are determined also by the ionospheric conductivity longitudinal gradients existing in association with the dawn and dusk terminators. Additionally, the *By* component of the IMF might also play a significant role in shaping the local time of the polarity reversal of the PPEF. For example, Chakrabarty et al. (2017) showed that the IMF *By* component under southward IMF *Bz* condition could skew the ionospheric equipotential pattern over the dip equator in such a way as to modify the local time of the polarity reversal of the PPEF. In any case the anomalously late time polarity reversal as found here merits further studies.

5. Concluding Remarks

We studied an interesting piece of observation that is related to the development of dawn sector EPB believed to be triggered by disturbance electric fields during a moderate geomagnetic storm on 4–5 February 2011. Observational data obtained from Gadanki VHF radar, a CADI ionosonde at Tirunelveli, and ASI at Kolhapur over Indian sector were analyzed together with solar wind data and the interplanetary and geomagnetic field parameters. These results demonstrate that even a minor geomagnetic storm can trigger fresh generation of plasma bubbles locally depending upon a combination of PPEF in possible presence of a DDEF. The results suggest that IMF *Bz* southward/northward transitions defining the different phases of the storm activity can cause irregularity generation in both the nighttime *E* and *F* regions. The Doppler velocities of the *E* region irregularities are found to respond sensitively to the polarities of the undershielding and overshielding electric fields and thereby serve as a reliable indicator of the *F* layer height changes in response to these electric fields. It was observed that under the *Bz* southward condition occurring till around midnight, the undershielding electric field that has eastward polarity (as expected from previous observational and model studies) caused *F* layer height increases resulting in SF irregularity development. More notably, it was observed that *Bz* southward transitions occurring well after midnight, that is, during presunrise hours, also can produce PPEF of eastward polarity, resulting in plasma bubble development, in contrast to the hitherto known/expected pattern. Thus, we note that presunrise development of plasma bubbles can occur under anomalous conditions of the penetration electric field. The present study shows further that the nighttime polarity reversal of the penetration electric field can occur at significantly later local time (by ~04 LT) than the latest reversal time reported so far (~00 LT). Another interesting result revealed from this study is that the topside irregularity plume height can be modulated in oscillatory pattern under correspondingly fluctuating IMF *Bz* values. Investigation needs to be pursued further to understand better the detailed characteristics and possible causative mechanisms responsible for the new findings reported in this paper.

Acknowledgments

The research work presented in this paper is carried out with the financial and infrastructure support from the Indian Institute of Geomagnetism (IIG), Navi Mumbai, which is an autonomous organization under the Department of Science and Technology (*DST*), India. The authors are thankful to technical staff at EGRL, Tirunelveli, for their support and dedication in operating ionosonde. Similarly, the authors would like to thank the technical staff at the National Atmospheric Research Laboratory (NARL), Gadanki, for their support in operating the MST radar. We also thank scientific personnel at WDC, Kyoto University, Japan, as well as Advanced Composition Explorer (ACE) satellite for providing geomagnetic indices such as *SYM-H* and *AE* (*AU*/*AL*) and interplanetary parameters such as solar wind and interplanetary magnetic fields (IMFs). The time-shifted solar data and other geomagnetic data are obtained from ftp://spdf.gsfc.nasa.gov/pub/data/omni/high_res_omni/. All the data mentioned in this paper are with the corresponding author, and he can be contacted at ssripathi.iig@gmail.com. M. A. A. acknowledges the support received from the Sao Paulo State Foundation for Promotion of Research (FAPESP) through the Process 2016/24970-7.

References

Aarons, J. (1991). The role of the ring current in the generation or inhibition of equatorial *F* layer irregularities during magnetic storms. *Radio Science*, *26*(4), 1131–1149. https://doi.org/10.1029/91RS00473

Abalde, J. R., Sahai, Y., Fagundes, P. R., Becker-Guedes, F., Bittencourt, J. A., Pillat, V. G., et al. (2009). Day-to-day variability in the development of plasma bubbles associated with geomagnetic disturbances. *Journal of Geophysical Research*, *114*, A04304. https://doi.org/10.1029/2008JA013788

Abdu, M. A. (2016). Electrodynamics of ionospheric weather over low latitudes. *Geoscience Letters*, *3*(1), 11. https://doi.org/10.1186/s40562-016-0043-6

Abdu, M. A., Batista, I. S., Sobral, J. H. A., Paula, E. R., & de Kantor, I. J. (1985). Equatorial ionospheric plasma bubble irregularity occurrence and zonal velocity under quiet and disturbed conditions, from Polarimeter observations. *Journal of Geophysical Research*, *90*, 9921–9928.

Abdu, M. A., Batista, I. S., Takahashi, H., MacGougall, J., Sobral, J. H., Medeiros, A. F., & Trivedi, N. B. (2003). Magnetospheric disturbance induced equatorial plasma bubble development and dynamics: A case study in Brazilian sector. *Journal of Geophysical Research*, *108*(A12), 1449. https://doi.org/10.1029/2002JA009721

Abdu, M. A., Kherani, E. A., Batista, I. S., & Sobral, J. H. A. (2009). Equatorial evening prereversal vertical drift and spread *F* suppression by disturbance penetration electric fields. *Geophysical Research Letters*, *36*, L19103. https://doi.org/10.1029/2009GL039919

Basu, S., Basu, S., Groves, K. M., Yeh, H.-C., Su, S.-Y., Rich, F. J., Sultan, P. J., et al. (2001). Response of the equatorial ionosphere in the South Atlantic region to the great magnetic storm of July 15, 2000. *Geophysical Research Letters*, *28*(18), 3577–3580. https://doi.org/10.1029/2001GL013259

Blanc, M., & Richmond, A. D. (1980). The ionospheric disturbance dynamo. *Journal of Geophysical Research*, *85*(A4), 1669. https://doi.org/10.1029/JA085iA04p01669

Chakrabarty, D., Sekar, R., Narayanan, R., Patra, A. K., & Devasia, C. V. (2006). Effects of interplanetary electric field on the development of an equatorial spread *F* event. *Journal of Geophysical Research*, *111*, A12316. https://doi.org/10.1029/2006JA011884

Chakrabarty, D., Hui, D., Rout, D., Sekar, R., Bhattacharyya, A., Reeves, G. D., & Ruohoniemi, J. M. (2017). Role of IMF By in the prompt electric field disturbances over equatorial ionosphere during a space weather event. *Journal of Geophysical Research: Space Physics*, *122*, 2574–2588. https://doi.org/10.1002/2016JA022781

Fejer, B. G. (1991). Low latitude electrodynamic plasma drifts: A review. *Journal of Atmospheric and Terrestrial Physics*, *53*(8), 677–693. https://doi.org/10.1016/0021-9169(91)90121-M

Fejer, B. G., Gonzales, C. A., Farley, D. T., Kelley, M. C., & Woodman, R. F. (1979). Equatorial electric fields during magnetically disturbed conditions 1. The effect of the interplanetary magnetic field. *Journal of Geophysical Research*, *84*(A10), 5797–5802. https://doi.org/10.1029/JA084iA10p05797

Fejer, B. G., Jensen, J. W., & Su, S. Y. (2008). Quiet time equatorial *F* vertical plasma drift model derived from ROCSAT-1 observations. *Journal of Geophysical Research*, *113*, A05304. https://doi.org/10.1029/2007JA012801

Fejer, B. G., & Kelley, M. C. (1980). Ionospheric irregularities. *Reviews of Geophysics and Space Physics*, *18*(2), 401–454. https://doi.org/10.1029/RG018i002p00401

Fejer, B. G., Spiro, R. W., Wolf, R. A., & Foster, J. C. (1990). Latitudinal variation of perturbation electric fields during magnetically disturbed periods: 1986 SUNDIAL observation and model results. *Annales de Geophysique*, *8*, 441–454.

Fukao, S., Ozawa, Y., Yamamoto, M., & Tsunoda, R. T. (2003). Altitude-extended equatorial spread *F* observed near sunrise terminator over Indonesia. *Geophysical Research Letters*, *30*(22), 2137. https://doi.org/10.1029/2003GL018383

Ghodpage, R. N., Taori, A., Patil, P. T., Gurubaran, S., Sripathi, S., Banola, S., & Sharma, A. K. (2014). Simultaneous optical measurements of equatorial plasma bubble (EPB) from Kolhapur (16.81°N, 74.21°E) and Gadanki (13.51°N, 79.21°E). *Journal of Atmospheric and Terrestrial Physics*, *121*, 196–205. https://doi.org/10.1016/j.jastp.2014.05.008i

Grant, I. F., MacDougall, J. W., Rouhniemi, J. M., Bristow, W. A., Sotko, G. J., Kocher, J. A., Danskin, D., et al. (1995). Comparison of plasma flow velocities determined by the ionosonde Doppler drift technique, Super DARN radars and patch motion. *Radio Science*, *30*(5), 1537–1549. https://doi.org/10.1029/95RS00831

Hines, C. O. (1960). Internal atmospheric gravity waves at ionospheric heights. *Canadian Journal of Physics*, *38*(11), 1441–1481. https://doi.org/10.1139/p60-150

Hysell, D. L., & Burcham, J. (1998). JULIA radar studies of equatorial spread *F*. *Journal of Geophysical Research*, *103*(A12), 29,155–29,167. https://doi.org/10.1029/98JA02655

Hysell, D. L., & Burcham, J. (2002). Long term studies of equatorial spread *F* using the JULIA radar at Jicamarca. *Journal of Atmospheric and Solar - Terrestrial Physics*, *64*(12-14), 1531–1543. https://doi.org/10.1016/S1364-6826(02)00091-3

Kelley, M. C. (1989). *The Earth's ionosphere: Plasma physics and electrodynamics*. San Diego, Calif: Academic Press.

Kelley, M. C., Fejer, B. G., & Gonzales, C. A. (1979). An explanation for anomalous ionospheric electric fields associated with a northward turning of the interplanetary magnetic field. *Geophysical Research Letters*, *6*(4), 301–304. https://doi.org/10.1029/GL006i004p00301

Kelley, M. C., Larsen, M. F., LaHoz, C., & McClure, J. P. (1981). Gravity wave initiation of equatorial spread *F*: A case study. *Journal of Geophysical Research*, *86*(A11), 9087–9100. https://doi.org/10.1029/JA086iA11p09087

Kelley, M. C., Makela, J. J., Beaujardiere, O., & Retterer, J. (2011). Convective ionospheric storms: A review. *Reviews of Geophysics*, *49*, RG2003. https://doi.org/10.1029/2010RG000340

Kintner, P. M., Kil, H., Beach, T. L., & de Paula, E. R. (2001). Fading timescales associated with GPS signal and potential consequences. *Radio Science*, *36*(4), 731–743. https://doi.org/10.1109/1999RS002310

Klostermeyer, J. (1969). Gravity waves in the *F* region. *Journal of Atmospheric and Solar-Terrestrial Physics*, *31*(1), 25–45. https://doi.org/10.1016/0021-9169(69)90079-8

Loewe, C. A., & Prölss, G. W. (1997). Classification and mean behavior of magnetic storms. *Journal of Geophysical Research*, *102*(A7), 14,209–14,213. https://doi.org/10.1029/96JA04020

Martinis, C. R., Mendillo, M. J., & Aarons, J. (2005). Toward a synthesis of equatorial spread *F* onset and suppression during geomagnetic storms. *Journal of Geophysical Research*, *110*, A07306. https://doi.org/10.1029/2003JA010362

Patra, A. K., Chaitanya, P. P., Dashora, N., Sivakandan, M., & Taori, A. (2016). Highly localized unique electrodynamics and plasma irregularities linked with the 17 March 2015 severe magnetic storm observed using multitechnique common-volume observations from Gadanki, India. *Journal of Geophysical Research: Space Physics*, *121*, 11,518–11,527. https://doi.org/10.1002/2016JA023384

Patra, A. K., Phanikumar, D. V., & Pant, T. K. (2009). Gadanki radar observations of *F* region field-aligned irregularities during June solstice of solar minimum: First results and preliminary analysis. *Journal of Geophysical Research*, *114*, A12305. https://doi.org/10.1029/2009JA014437

Paulino, I., Medeiros, A. F., Buriti, R. A., Sobral, J. H. A., Takahashi, H., & Gobbi, D. (2010). Optical observations of plasma bubble westward drifts over Brazilian tropical region. *Journal of Atmospheric and Solar - Terrestrial Physics*, *72*(5-6), 521–527. https://doi.org/10.1016/j.jastp.2010.01.015

Picone, J. M., Hedin, A. E., Drob, D. P., & Aikin, A. C. (2002). NRLMSISE-00 empirical model of the atmosphere: Statistical comparisons and scientific issues. *Journal of Geophysical Research*, *107*(A12), SIA 15-1–SIA 15-16. https://doi.org/10.1029/2002JA009430

Pimenta, A. A., Sahai, Y., Bittencourt, J. A., & Rich, F. J. (2007). Ionospheric plasma blobs observed by OI 630 nm all-sky imaging in the Brazilian tropical sector during the major geomagnetic storm of April 6–7, 2000. *Geophysical Research Letters*, *34*, L02820. https://doi.org/10.1029/2006GL028529

Ram, S., Ajith, K. K., Yamamoto, M., Otsuka, Y., Yokoyama, T., Niranjan, K., & Gurubaran, S. (2015). Fresh and evolutionary-type field-aligned irregularities generated near sunrise terminator due to overshielding electric fields. *Journal of Geophysical Research: Space Physics*, *120*, 5922–5930. https://doi.org/10.1002/2015JA021427

Ramsingh, Sripathi, S., Sreekumar, S., Banola, S., Emperumal, K., Tiwari, P., & Kumar, B. S. (2015). Low-latitude ionosphere response to super geomagnetic storm of 17/18 March 2015: Results from a chain of ground-based observations over Indian sector. *Journal of Geophysical Research: Space Physics*, *120*, 10,864–10,882. https://doi.org/10.1002/2015JA021509

Rao, P. B., Jain, A. R., Kishore, P., Balamuralidhar, P., Damle, S. H., & Viswanathan, G. (1995). Indian MST radar, 1. System description and sample vector wind measurements in ST mode. *Radio Science*, *30*(4), 1125–1138. https://doi.org/10.1029/95RS00787

Senior, C., & Blanc, M. (1984). On the control of magnetospheric convection by the spatial distribution of ionospheric conductivities. *Journal of Geophysical Research*, *89*(A1), 261–284. https://doi.org/10.1029/JA089iA01p00261

Sripathi, S., Bose, S., Patra, A. K., Pant, T. K., Kakad, B., & Bhattacharyya, A. (2008). Simultaneous observations of ESF irregularities over Indian region using radar and GPS. *Annales de Geophysique*, *26*(11), 3197–3213. https://doi.org/10.5194/angeo-26-3197-2008

Sripathi, S., Singh, R., Banola, S., Sreekumar, S., Emperumal, K., & Selvaraj, C. (2016). Characteristics of the equatorial plasma drifts as obtained by using Canadian Doppler ionosonde over southern tip of India. *Journal of Geophysical Research: Space Physics*, *121*, 8103–8120. https://doi.org/10.1002/2016JA023088

Subbarao, K. S. V., & Krishna Murthy, B. V. K. (1994). Seasonal variations of equatorial spread *F*. *Annales de Geophysique*, *12*, 33.

Woodman, R. F., & LaHoz, C. (1976). Radar observations of *F* region equatorial irregularities. *Journal of Geophysical Research*, *81*(31), 5447–5466. https://doi.org/10.1029/JA081i031p05447

Zalesak, S. T., Ossakow, S. L., & Chaturvedi, P. K. (1982). Nonlinear equatorial spread *F*: The effect of neutral winds and background Pedersen conductivity. *Journal of Geophysical Research*, *87*(A1), 151–166. https://doi.org/10.1029/JA087iA01p00151